JOURNAL OF GUIDANCE, CONTROL, AND DYNAMICS
Vol. 33, No. 2, March–April 2010

Highly Constrained Optimal Launch Ascent Guidance

Ping Lu*
Iowa State University, Ames, Iowa 50011-2271
and
Binfeng Pan†
Northwestern Polytechnical University, 711072 Xi'an, People's Republic of China

DOI: 10.2514/1.45632

This paper is concerned with ascent guidance of multiple-stage launch vehicles subject to aerodynamic bending-moment constraint. In the first part of the paper, several new developments are made to refine and expand the capability of an optimal endoatmospheric ascent-guidance algorithm. These include new conditions for determining optimal body axes of the vehicle, handling of the aerodynamic bending-moment constraint by automated optimization of gravity-turn trajectory or by optimal closed-loop guidance, and seamless integration of the endoatmospheric guidance algorithm with exoatmospheric ascent-guidance algorithm for the upper stages of a vehicle. An extensive application of these developments using the vehicle and mission data of the Ares I Crew Launch Vehicle constitutes the second part of the paper. Extensive Monte Carlo simulations are conducted to demonstrate the algorithm and compare optimal closed-loop ascent guidance with conventional open-loop ascent guidance. The testing results help answer an age-old question on the comparison of closed-loop and open-loop ascent guidance on performance and constraint enforcement in the presence of winds and dispersions.

I. Introduction

ASCENT through the dense atmosphere remains the most challenging phase of operation for launch vehicles. This is the phase in which the direction and magnitude of the aerodynamic forces are tightly coupled with the direction of the propulsive force. Trajectory constraints due to aerodynamic loads and winds must be satisfied during this phase for the safety and integrity of the vehicle. Within the subspace allowed by the constraints, the ascent trajectory must be *optimized*, because the alternative (nonoptimal trajectories) could easily result in significantly reduced injected payload mass. Historically, endoatmospheric ascent guidance has been *open-loop*, due in no small part to the great difficulty in meeting these competing requirements reliably by a real-time optimal guidance algorithm in the presence of aerodynamic forces and winds. Take the current Ares I Crew Launch Vehicle (CLV) as a case in point. The CLV is a key component of NASA's Constellation Program. The vehicle has a very long, slender configuration. The aerodynamic bending moment is an important concern during its atmospheric ascent. Therefore, the Ares I is steered to fly a gravity turn moments after liftoff, which amounts to constraining the total angle of attack to zero in the nominal trajectory. The standard endoatmospheric ascent-guidance approach is to optimize the maneuvers of the vehicle offline, before it enters the gravity turn. The guidance commands are then extracted from the trajectory optimization result and loaded into the vehicle for open-loop guidance. Reference [1] contains more detailed description of the time-consuming and labor-intensive nature of this process. The steering for the second stage is by optimal closed-loop exoatmospheric guidance, as the aerodynamic forces greatly diminish after the first stage.

As a continuing effort toward developing a robust and fast algorithm for automated ascent planning and toward the ultimate realization of optimal closed-loop endoatmospheric ascent guidance, a goal pursued since the early 1970s [2–13], this paper contains two main related components that are motivated by and directly geared toward the applications such as that for the Ares I. The first is further refinement and expansion of capability of an optimal endoatmospheric guidance algorithm, which is first presented in [9]. Developments are made in several aspects. New conditions are presented that determine the optimal body axes in heads-down launch ascent, which has not been considered before in the literature. A focus of this paper is the handling of the aerodynamic bending-moment constraint in the form of an inequality constraint on $\alpha_t\bar{q}$, where α_t is the total angle of attack and $\bar{q}$ is the dynamic pressure. The algorithm reported in [9] is expanded to allow automated design of optimized gravity-turn trajectories. Traditional open-loop ascent-guidance commands for endoatmospheric flight can be directly extracted from such a solution. Alternatively, incorporating the inequality constraint on $\alpha_t\bar{q}$ into the optimal solution and repeatedly solving the optimal control problem online realizes closed-loop guidance. The endoatmospheric ascent algorithm is expanded to offer just such a capability. For multiple-stage launch vehicles, a new seamless integration of the endo- and exoatmospheric guidance algorithms is presented. This new integration approach avoids some of the drawbacks of the previous method [11], further enhances the reliability of the algorithm, and reduces the number of guidance initialization loads (I-loads).

As the second main component of the paper and for an in-depth demonstration, all the developments reported in the paper are applied using the Ares I vehicle and its mission profile to the International Space Station. Extensive closed-loop simulation testing with realistic propulsion dispersions and winds is conducted to evaluate and demonstrate the efficacy of the method and algorithm developed in this paper. In conjunction with the ascent-guidance comparison using Ares I data, we revisit an age-old question in launch guidance: that is, how optimal closed-loop endoatmospheric ascent guidance compares with traditional open-loop endoatmospheric ascent guidance. Hanson et al. [14] make a first effort to compare closed-loop and open-loop guidance inside the atmosphere. They find that optimal closed-loop guidance performs slightly better than open-loop guidance when no $\alpha_t\bar{q}$ constraint is imposed. When load relief is implemented to enforce the $\alpha_t\bar{q}$ constraint, closed-loop ascent guidance is actually found to fair somewhat worse than open-loop guidance. We believe that we have identified the root cause for this

---

Presented as Paper 5961 at the Guidance, Navigation, and Control Conference, Chicago, IL, 10–13 August 2009; received 25 May 2009; revision received 28 November 2009; accepted for publication 1 December 2009.

*Professor, Department of Aerospace Engineering, 2271 Howe Hall; plu@iastate.edu, Associate Fellow AIAA.

†Currently Visiting Graduate Student, Iowa State University; panbinfeng@gmail.com.

seemingly contradictory finding (that optimal closed-loop guidance performs worse than open-loop guidance that is not strictly optimal in the presence of any dispersions). The key lies in how the $\alpha_t\bar{q}$ constraint is treated in closed-loop guidance. For algorithm simplicity, this constraint is usually checked and enforced, when necessary, after the *unconstrained* optimal solution has been found. The underlying justification is that such a posterior treatment will cause relatively small performance degradation. However, we find that for truly optimal performance, it is important to include the $\alpha_t\bar{q}$ constraint in the optimal solution process by strictly following the necessary conditions of optimality. With the algorithm described in this paper, we are in a unique position to offer a set of comparative studies on ascent-guidance approaches through extensive Monte Carlo simulations using the Ares I vehicle and mission data.

Judged by performance in terms of injected mass and by enforcement of the constraint on $\alpha_t\bar{q}$, our results clearly show that in the presence of winds and vehicle modeling dispersions, optimal closed-loop guidance yields better overall performance, and the conventional open-loop guidance produces statistically lower injected mass. Another important finding is that closed-loop guidance is able to keep the $\alpha_t\bar{q}$ constraint safely satisfied even in the presence of larger dispersions, whereas open-loop guidance may not guarantee this. Indeed, in some of the large-dispersion cases, the violations of the $\alpha_t\bar{q}$ constraint under open-loop guidance are found to be substantial.

II. Optimal Endoatmospheric Ascent Problem

A. Ascent Dynamics

The equations of motion of a rocket ascending through the atmosphere can be expressed in an inertial frame as

$$\dot{\boldsymbol{r}} = \boldsymbol{V} \tag{1}$$

$$\dot{\boldsymbol{V}} = \boldsymbol{g}(\boldsymbol{r}) + \frac{\mathbf{A}}{m(t)} + \frac{T\mathbf{1}_b}{m(t)} + \frac{\mathbf{N}}{m(t)} \tag{2}$$

$$\dot{m} = -\eta(t) \tag{3}$$

where $\boldsymbol{r} \in R^3$ and $\boldsymbol{V} \in R^3$ are the position and inertial velocity vectors; $\boldsymbol{g}$ is the gravitational acceleration; and T is the current thrust magnitude, including effects of throttle modulation, if applicable, and thrust loss due to back pressure. In this formulation, the total engine thrust is assumed to be aligned with the body longitudinal axis. Any effects due to gimballing of the thrust vector for attitude control are assumed to be small and are ignored for trajectory-generation purposes. However, the following development remains applicable even if the thrust vector is not aligned with the body longitudinal axis but is slanted at a constant angle. The vectors $\mathbf{A}$ and $\mathbf{N}$ are the aerodynamic forces in the body longitudinal and normal directions, respectively; $\mathbf{1}_b$ is the unit vector defining the rocket body longitudinal axis. This is the *zero-sideslip* formulation in which the vehicle body attitude is chosen so that the symmetric plane will contain the wind-relative velocity vector. The mass of the vehicle at the current time t is $m(t)$. The mass flow rate of the rocket is $\eta(t) > 0$, which is a function of time for solid rocket motors; for liquid propellant rockets, $\eta(t)$ may be closely approximated by a constant for given throttle. The initial condition $(\boldsymbol{r}(t_0),\ \boldsymbol{V}(t_0),\ m(t_0))$ is given. For better numerical conditioning, the following normalization is used:

1) The distances are normalized by R_0, the radius of the Earth at the equator.

2) Time is normalized by $\sqrt{R_0/g_0}$, where g_0 is the gravitational acceleration at R_0.

3) The velocities are normalized by $\sqrt{R_0 g_0}$, the circular velocity around the Earth at R_0.

The gravity is modeled by the Newtonian central gravity field. Still using the same names hereafter for the dimensionless variables, we have the dimensionless equations of motion from Eqs. (1) and (2):

$$\boldsymbol{r}' = \boldsymbol{V} \tag{4}$$

$$\boldsymbol{V}' = -\frac{1}{r^3}\boldsymbol{r} + \mathbf{A} + T\mathbf{1}_b + \mathbf{N}, \qquad \|\mathbf{1}_b\| = 1 \tag{5}$$

where prime indicates differentiation with respect to the dimensionless time; $\mathbf{A}$ and $\mathbf{N}$ are the aerodynamic accelerations in the units of g_0, in the body longitudinal and normal directions, respectively; and T is the magnitude of the thrust acceleration in g_0. Define the dimensionless wind-relative velocity

$$\boldsymbol{V}_r = \boldsymbol{V} - \bar{\omega}_E \times \boldsymbol{r} - \boldsymbol{V}_w \tag{6}$$

where $\bar{\omega}_E$ is the Earth angular rotation rate vector normalized by $\sqrt{g_0/R_0}$, and $\boldsymbol{V}_w$ is the dimensionless wind velocity. The magnitudes of the dimensionless aerodynamic and thrust accelerations are given by

$$A = R_0\rho(r)V_r^2 S_{\text{ref}} C_A(\text{Mach}, \alpha)/2m(t) \tag{7}$$

$$N = R_0\rho(r)V_r^2 S_{\text{ref}} C_N(\text{Mach}, \alpha)/2m(t) \tag{8}$$

$$T = [T_{\text{vac}} - S_{\text{exit}}\,p(r)]/m(t)g_0 \tag{9}$$

where $V_r = \|\boldsymbol{V}_r\|$. The axial and normal aerodynamic coefficients C_A and C_N are functions of angle of attack α and Mach number. The rest of the quantities in the above three equations are all dimensional: $\rho(r)$ is the atmospheric density at radius r, S_{ref} is the vehicle's reference area, T_{vac} is the vacuum thrust, S_{exit} is the engine nozzle exit area, and $p(r)$ is the ambient atmospheric pressure at r. Denote the body-normal unit vector by $\mathbf{1}_N$. Then the aerodynamic force (acceleration) vectors are

$$\mathbf{A} = -A\mathbf{1}_b, \qquad \mathbf{N} = N\mathbf{1}_N \tag{10}$$

Note that not only do the directions of $\mathbf{A}$ and $\mathbf{N}$ depend on $\mathbf{1}_b$, but so do their magnitudes, through their dependence on α.

B. Necessary Conditions

The performance index of the optimal ascent problem is the minimization of

$$J = \int_{t_0}^{t_f} \eta(t)\,\mathrm{d}t \tag{11}$$

where t_f is the orbital insertion time to be determined. For given initial mass $m(t_0)$, this performance index is equivalent to maximizing the insertion mass. The final insertion conditions are defined by k equations with $0 < k \leq 6$, put together in vector form:

$$\boldsymbol{\psi}(\boldsymbol{r}_f, \quad \boldsymbol{V}_f) = 0 \tag{12}$$

where $\boldsymbol{r}_f$ and $\boldsymbol{V}_f$ are the position and inertial velocity vectors of the vehicle at t_f. The optimal control problem amounts to finding the optimal body attitude history $\mathbf{1}_b(t)$, such that, from the specified initial condition, the solution of the dynamic equations in the preceding section satisfies the terminal constraint in Eq. (12) and the performance index (11) is minimized. Note that no inequality constraints on the ascent trajectory are considered yet; they will be addressed later. From the optimal control theory, define the Hamiltonian

$$H = \boldsymbol{p}_r^T\boldsymbol{V} + \boldsymbol{p}_V^T\left[-\frac{1}{r^3}\boldsymbol{r} + (T - A)\mathbf{1}_b + N\mathbf{1}_N\right] - \eta(t) \tag{13}$$

where $\boldsymbol{p}_r \in R^3$ and $\boldsymbol{p}_V \in R^3$ are the costate vectors. Let an asterisk denote the optimal value of a variable. The standard necessary conditions for the optimal solution require

$$\boldsymbol{p}'_r = -\frac{\partial H}{\partial \boldsymbol{r}} \tag{14}$$

$$\boldsymbol{p}'_V = -\frac{\partial H}{\partial \boldsymbol{V}} \tag{15}$$

$$H(\boldsymbol{p}_r, \boldsymbol{p}_V, \boldsymbol{r}^*, \boldsymbol{V}^*, \mathbf{1}_b^*, t) = \max_{\mathbf{1}_b} H(\boldsymbol{p}_r, \boldsymbol{p}_V, \boldsymbol{r}^*, \boldsymbol{V}^*, \mathbf{1}_b, t) \tag{16}$$

The detailed expressions of the vector costate equations (14) and (15) are fairly involved and can be found in [9]. It is argued in [7], and later analytically shown in [9], that the optimality condition (16) necessitates the optimal $\mathbf{1}_b(t)$ axis to lie in the plane formed by the relative velocity vector $\boldsymbol{V}_r(t)$ and the primer vector $\boldsymbol{p}_V(t)$. Figure 1 illustrates this outcome, and case 1 is first shown in [7]. In this plane, the orientation of the optimal $\mathbf{1}_b$ is defined by a single parameter. A most convenient choice is the angle between $\mathbf{1}_b$ and $\boldsymbol{V}_r$, which is the angle of attack. Therefore, the optimality condition (16) is reduced to

$$\frac{\partial H}{\partial \alpha} = 0 \tag{17}$$

In the next section, it will be clear that the solution to Eq. (17) only depends on $\boldsymbol{p}_V$ at any given state and thrust. Now recall the zero-sideslip requirement in the problem formulation. This means that the plane formed by $\boldsymbol{V}_r(t)$ and $\boldsymbol{p}_V(t)$ is the symmetric plane of the vehicle. Thus, at any given state, $\boldsymbol{p}_V$ contains all the information needed to determine the optimal body axes.

The role of the costate vector $\boldsymbol{p}_V$ in optimal trajectories of rockets in exoatmospheric flight is well understood: the optimal thrust direction is in the same direction of $\boldsymbol{p}_V$. For this reason, Lawden [15] calls $\boldsymbol{p}_V$ the primer vector. From the quick exposition above, the critical importance of $\boldsymbol{p}_V(t)$ in the solution of optimal endoatmospheric ascent trajectory henceforth is also apparent, even though the relationship between the optimal thrust direction (defined by $\mathbf{1}_b$) and $\boldsymbol{p}_V$ is more complex in endoatmospheric flight.

III. Optimal Body Axes

In optimal endoatmospheric flight, the optimal body x-axis unit vector $\mathbf{1}_b$ determined from Eq. (17) will not align with $\boldsymbol{p}_V$ in general. But as will be shown subsequently, the optimal $\mathbf{1}_b$ is still uniquely determined by the primer vector $\boldsymbol{p}_V$ at any given state and thrust level, albeit in a more complex way. Using a correct form of Eq. (17) to solve for α, thus determining the direction of the optimal $\mathbf{1}_b$, turns out to be a problem that warrants some careful analysis. Once $\mathbf{1}_b$ is found, an ambiguity still exists: that is, the body y axis can be in either of the two opposite directions that are perpendicular to the $\boldsymbol{V}_r$–$\boldsymbol{p}_V$ plane. Consequently, the unit body-normal vector $\mathbf{1}_N$ (where $\mathbf{1}_N = -\mathbf{1}_z$ with $\mathbf{1}_z$ representing the unit vector of the body z axis) can be in one of the two collinear directions shown in Fig. 1. Let us consider both cases in the following.

A. Case 1: Heads-Up Ascent

This is the case in which $\mathbf{1}_N$ is shown with a solid line in Fig. 1. Define the control Hamiltonian as

$$H_c = \mathbf{1}_{p_V}^T \mathbf{1}_b (T - A) + \mathbf{1}_{p_V}^T \mathbf{1}_N N \tag{18}$$

where $\mathbf{1}_{p_V} = \boldsymbol{p}_V / \|\boldsymbol{p}_V\|$. Condition (17) is clearly the same as $\partial H_c / \partial \alpha = 0$. When $\mathbf{1}_N$ is in the solid-line direction (case 1) in Fig. 1, it is obvious that

$$H_c = \cos(\Phi - \alpha)(T - A) + N \sin(\Phi - \alpha) \tag{19}$$

where $\Phi = \cos^{-1}(\mathbf{1}_{p_V}^T \mathbf{1}_{V_r}) > 0$ is the angle between $\mathbf{1}_{p_V}$ and $\mathbf{1}_{V_r}$, always taken to be nonnegative and no greater than π. The condition $\partial H_c / \partial \alpha = 0$ yields

$$\tan(\Phi - \alpha)(T - A + N_\alpha) - (A_\alpha + N) = 0 \tag{20}$$

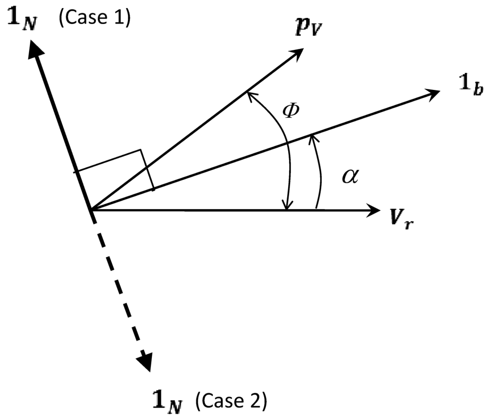

Fig. 1 Optimal launch vehicle body axes.

where $N_\alpha = \partial N / \partial \alpha$ and $A_\alpha = \partial A / \partial \alpha$. Once α is found from Eq. (20), it can be readily shown that the optimal $\mathbf{1}_b$ is given by

$$\mathbf{1}_b = \frac{\sin \alpha}{\sin \Phi} \mathbf{1}_{p_V} + \frac{\sin(\Phi - \alpha)}{\sin \Phi} \mathbf{1}_{V_r} \tag{21}$$

where $\mathbf{1}_{V_r} = \boldsymbol{V}_r / \|\boldsymbol{V}_r\|$. Note that as the atmospheric density decreases (approaching vacuum flight), the aerodynamic terms diminish, and $\alpha \to \Phi$ from Eq. (20). The optimal body x axis in Eq. (21) and, therefore, the optimal thrust vector become aligned with the primer vector $\boldsymbol{p}_V$ [15]. The unit vector of the body y axis in the zero-sideslip formulation corresponding to this case is determined by

$$\mathbf{1}_y = \frac{\mathbf{1}_{V_r} \times \mathbf{1}_{p_V}}{\|\mathbf{1}_{V_r} \times \mathbf{1}_{p_V}\|} \tag{22}$$

If the wing-level formulation in [12] is to be used, the body y axis is then defined by

$$\mathbf{1}_y = \frac{\mathbf{1}_b \times \boldsymbol{r}}{\|\mathbf{1}_b \times \boldsymbol{r}\|} \tag{23}$$

Note that the wing-level definition of $\mathbf{1}_y$ in above equation is approximately optimal in that the side aerodynamic force is assumed to be small (see [12] for more detail in this regard).

B. Case 2: Heads-Down Ascent

When $\mathbf{1}_N$ is in the dashed-line direction in Fig. 1 (case 2), H_c defined in Eq. (18) becomes

$$H_c = \cos(\Phi + \alpha)(T - A) - N \sin(\Phi + \alpha) \tag{24}$$

Note that α as shown in Fig. 1 is negative in this case. The condition $\partial H_c / \partial \alpha = 0$ leads to

$$\tan(\Phi + \alpha)(T - A + N_\alpha) + (A_\alpha + N) = 0 \tag{25}$$

With α found, the optimal $\mathbf{1}_b$ in this case can be shown to be given by

$$\mathbf{1}_b = -\frac{\sin \alpha}{\sin \Phi} \mathbf{1}_{p_V} + \frac{\sin(\Phi + \alpha)}{\sin \Phi} \mathbf{1}_{V_r} \tag{26}$$

The body y axis in zero-sideslip configuration corresponding to $\mathbf{1}_b$ above is determined by

$$\mathbf{1}_y = \frac{\mathbf{1}_{p_V} \times \mathbf{1}_{V_r}}{\|\mathbf{1}_{p_V} \times \mathbf{1}_{V_r}\|} \tag{27}$$

Similarly, the body y axis in wing-level configuration is given by

$$\mathbf{1}_y = \frac{\boldsymbol{r} \times \mathbf{1}_b}{\|\boldsymbol{r} \times \mathbf{1}_b\|} \tag{28}$$

Note the opposite directions of $\mathbf{1}_y$ in Eq. (22) [or Eq. (23)] and Eq. (27) [or Eq. (28)]. As the atmospheric density decreases (thus,

$A \to 0$ and $N \to 0$), $\alpha \to -\Phi$ from Eq. (25). The optimal body x axis in Eq. (26) and the optimal thrust vector again become aligned with the primer vector $\boldsymbol{p}_V$. The fact that $\alpha \to -\Phi < 0$ indicates that in this configuration, α tends to be negative (although positive values for α in the early part of the endoatmospheric ascent are still possible). If the launch vehicle is completely aerodynamically symmetric with respect to the angle of attack α, then $N(-\alpha) = -N(\alpha)$, $A(-\alpha) = A(\alpha)$, $N_\alpha(-\alpha) = N_\alpha(\alpha)$, and $A_\alpha(-\alpha) = -A_\alpha(\alpha)$. For such a vehicle, it is evident that if α is the solution to Eq. (20), then $-\alpha$ will be the solution to Eq. (25), and the body x axes from Eqs. (21) and (26) are the same. Consequently the optimal ascent trajectory will be the same whether it is a heads-up or heads-down launch, but α has opposite sign. Note that even for symmetric vehicles, the equations in case 2 are still needed in order to determine the correct sign of α and body axes for heads-down launch. If the vehicle is not aerodynamically symmetric with respect to α, the two α solutions to Eqs. (20) and (25) are. in general, different in magnitude and possibly in sign, and the optimal body axes from Eqs. (21) and (26) will differ. As a result, the corresponding ascent trajectories (and injected masses) will be different.

It should be pointed out that the discussion about case 2 above has not been reported in the literature before, including [9], probably because it was thought to be already included in case 1. In [9] there is a discussion of when the sign of Φ should be set to be negative, and α is always solved from Eq. (20). It can be shown that if Φ is taken to be negative, then $-\alpha$ is the solution to Eq. (20) for a symmetric vehicle. But the logic in [9] of when to set Φ to negative is contrived and, per the above discussion, it does not provide a correct solution for asymmetric vehicles. The above development is much cleaner and easier to apply.

The choice of heads-up or heads-down launch is based on a number of considerations, including communication, visibility for crew, and performance. For an axially asymmetric vehicle, if the two solutions yield a performance differential in terms of the injected mass that is deemed substantial, the finding could serve as a factor for deciding which launch orientation of the vehicle to use.

IV. Optimal Ascent Constrained by Aerodynamic Bending Moment

The bending moment due to aerodynamic force is of an important concern in the launch of slender vehicles. A case in point is the Ares I vehicle, which is over 300 ft in length. The bending-moment constraint is typically in the form of an inequality constraint:

$$\alpha_t \bar{q} \le n_{q_{\max}} \tag{29}$$

where α_t is the total angle of attack (the angle between the body x axis and the wind-relative velocity vector $\boldsymbol{V}_r$), $\bar{q}$ is the dynamic pressure, and $n_{q_{\max}}$ is a specified value. Note that α_t is equal to α when the sideslip angle is zero. Traditionally, the guidance strategy in such a case is to design the ascent trajectory to fly a gravity turn in which the nominal angle of attack is zero. For instance, to limit the bending moment during endoatmospheric ascent, the Ares I is steered optimally to latch onto a gravity-turn trajectory shortly after clearing the tower [1]. The maneuvers to transition from initial vertical ascent to the gravity-turn trajectory are optimized offline and the command profiles are then loaded onboard for guidance. This process is laborious and time-consuming. A simplified and effective optimization procedure is developed by Dukeman and Hill [1], in which a constant pitch rate and desired trajectory azimuth are optimized to achieve essentially the same performance. The optimality of these initial maneuvers is critically important for performance, as the subsequent trajectory is highly constrained.

Our numerical algorithm is based on the relaxation method described in [9] for endoatmospheric portion and on the analytical method described in [16] for exoatmospheric flight. Improved integration of the two algorithms will be discussed in Sec. V. The integrated algorithm can be easily modified to automatically incorporate the design of the optimal pitch and yaw maneuvers to fly onto a gravity-turn trajectory during the endoatmospheric ascent, without need for human interference and input.

The issue of guidance is closely related. If the endoatmospheric guidance is to be conventional open-loop guidance, the guidance commands are extracted from the optimized trajectory for onboard applications. If optimal closed-loop guidance is to be employed, the guidance solution should maximize the injected mass while enforcing the constraint in Eq. (29), based on the state of the trajectory in every guidance cycle. In this section, the modifications to the algorithm that enable optimal constrained closed-loop guidance are also discussed.

A. Optimal Gravity-Turn Trajectory Planning

Let t_1 be the known time since liftoff when the launch vehicle clears the tower, and let $t_2 > t_1$ be the specified time when the gravity turn is to begin. For the Ares I, $t_1 = 6$ s and $t_2 = 23.3$ s are used in [1]. In trajectory planning, the algorithm uses Eqs. (20–22) or Eqs. (25–27) in the time interval $[t_1, t_2]$ to determine the optimal maneuvers. For $t > t_2$ until the burnout of the first stage, a fixed $\alpha = 0$ is used; thus, $\mathbf{1}_b = \mathbf{1}_{V_r}$. The costate equations (14) and (15) are still being propagated, and the body y axis is still determined by either Eq. (22) or Eq. (27). Methodologically, this process is equivalent to dividing the endoatmospheric (first-stage) flight after the clearance of the launch tower into two phases in which dynamic equations differ. The separation condition of the two phases is defined by an interior-point constraint:

$$\varphi(t) = t - t_2 = 0 \tag{30}$$

In the first phase in $[t_1, \ t_2]$, the trajectory dynamics are those in Eqs. (4) and (5), and $\mathbf{1}_b$ is optimized. In the second phase in $[t_2, \ t_{cf}]$, where t_{cf} is the first-stage engine cutoff time, the trajectory dynamics are

$$\boldsymbol{r}' = \boldsymbol{V} \tag{31}$$

$$\boldsymbol{V}' = -\frac{1}{r^3}\boldsymbol{r} + (T - A)\mathbf{1}_{V_r} \tag{32}$$

By the theory of optimal control [17], the state and costate remain continuous at t_2, but the Hamiltonian H will satisfy a jump condition at t_2:

$$H(t_2^+) = H(t_2^-) + \nu \frac{\partial \varphi(t_2)}{\partial t} = H(t_2^-) + \nu \tag{33}$$

where ν is a multiplier. Since the interior values of H are not explicitly used in the implementation of the algorithm, there is no need to find ν. Therefore, such a division of phases does not introduce any additional unknowns or complexity, but it does offer a formal interpretation within the framework of optimal control theory to the pre-gravity-turn optimization in $[t_1, \ t_2]$ and gravity turn in $[t_2, \ t_{cf}]$.

The algorithm typically finds the solution very rapidly (on the order of 0.05 s on a typical desktop computer). The resulting (open-loop) trajectory will be in gravity turn after t_2, and the maneuvers in $[t_1, \ t_2]$ are optimized.

Another way to treat this problem is to keep the same dynamics as in Eqs. (4) and (5) for both phases in $[t_1, \ t_2]$ and $[t_2, \ t_{cf}]$. But in the second phase, an inequality constraint is imposed on the trajectory:

$$\alpha_t \bar{q} \le 0 \tag{34}$$

The above constraint is equivalent to $\alpha_t = 0$ (the total angle of attack α_t is taken to be nonnegative). With the presence of this constraint, the optimal trajectory can be handled in the same way as described in the next section. In this way, the same software can used to either design the optimized gravity-turn ascent trajectory or to perform closed-loop guidance, as elaborated in the following.

B. Optimal Closed-Loop Guidance

Optimal closed-loop guidance in the presence of constraint equation (29) requires that the optimal solution of the ascent problem should explicitly include the enforcement of constraint equation (29), and the solution is repeated onboard in each guidance cycle with the current actual state as the initial condition. Rewrite the constraint equation (29) as

$$S_1 = \alpha_t \bar{q} - n_{q_{\max}} \leq 0 \tag{35}$$

This constraint is a zeroth-order constraint in that the control $\mathbf{1}_b$ appears explicitly (through α_t) in the constraint itself. The subsequent development follows standard optimal control theory for problems subject to zeroth-order inequality constraints. In the presence of constraint (35), the costate equations take the form of

$$\boldsymbol{p}' = -\frac{\partial H}{\partial \boldsymbol{x}} - \lambda \frac{\partial S_1}{\partial \boldsymbol{x}} \tag{36}$$

where $\boldsymbol{p} = (\,\boldsymbol{p}_r^T \quad \boldsymbol{p}_V^T\,)^T$ and $\boldsymbol{x} = (\,\boldsymbol{r}^T \quad \boldsymbol{V}^T\,)^T$. The multiplier $\lambda = 0$ and the problem reduces to the unconstrained one when $S_1 < 0$. For zero sideslip, $\alpha_t = \alpha$. It can be shown that in the case when $S_1 \leq 0$ is active, the conclusion alluded to in Sec. II.B is still valid: the optimal body axis $\mathbf{1}_b$ lies in the plane of $\boldsymbol{p}_V$ and $\boldsymbol{V}_r$ (see [9] for more details). In the finite time interval when $S_1 = 0$, the optimality condition becomes

$$\frac{\partial H}{\partial \alpha} + \lambda \frac{\partial S_1}{\partial \alpha} = 0 \tag{37}$$

In this interval, α is directly obtained from $S_1 = 0$:

$$\alpha = n_{q_{\max}} / \bar{q} \tag{38}$$

With this α, the optimal body axis $\mathbf{1}_b$ is determined by Eq. (21) or Eq. (26) as before. The multiplier λ is calculated from Eq. (37):

$$\lambda = -\frac{\partial H / \partial \alpha}{\partial S_1 / \partial \alpha} = -\frac{\partial H / \partial \alpha}{\bar{q}} \tag{39}$$

where $\partial H / \partial \alpha = \partial H_c / \partial \alpha$ with H_c defined in Eq. (19) or Eq. (24). Note that $\partial H_c / \partial \alpha$ will have different signs, depending on heads-up or heads-down launch. This λ from Eq. (39) is then used in the costate equation (36) to propagate the costate in the interval in which S_1 is active.

In short summary, when the bending-moment constraint (29) is active, the differences in the solution process of the optimal control problem are in costate equation (36) and how α is determined [from Eq. (38)]. But there are no additional unknown variables/multipliers that will increase the computational difficulty.

For simplicity of the algorithm, the temptation is to solve for the unconstrained solution without regard to constraint (29) first, then in applying the guidance commands, treat Eq. (29) as a saturating limit on α_t found from unconstrained trajectory and adjust the commanded body axes accordingly. Such an approach is not advisable. This is because simply limiting $\alpha_t \leq n_{q_{\max}} / \bar{q}$ as an afterthought without the unconstrained solution being reasonably close to the constrained solution would likely cause convergence problems in subsequent guidance cycles. Even when the convergence problems are overcome, the resulting trajectory could still suffer considerable performance loss in terms of injected mass, since such a posterior treatment has no guarantee of optimality of any sort. Indeed, our tests with this engineering approach in the Monte Carlo simulations to be reported in Sec. VI.C result in substantial performance degradation. In contrast, the above handling of the constraint (29) is rigorous by following the necessary conditions in optimal control theory [9,13].

It should be noted that the above optimal closed-loop guidance does not steer the vehicle to fly a strict gravity-turn trajectory. Thus, the angle of attack will not be zero for an extended period as in gravity turn, but it will remain small. This closed-loop guidance can be activated right after the vehicle clears the launch tower.

V. Integration of Endo- and Exoatmospheric Guidance Algorithms

Even though an atmospheric optimal ascent algorithm will work in principle for exoatmospheric flight, the code is much more complex than necessary for guidance of upper stages. In addition, exoatmospheric ascent-guidance algorithm is typically also a part of on-orbit guidance software, which is required to be more flexible in handling various other tasks. Therefore, exoatmospheric ascent guidance for the upper stages of a multiple-stage vehicle is best left for an algorithm specifically designed for space flight. The use of different algorithms for endo- and exoatmospheric ascents gives rise to the need for integrating the two algorithms so that a complete end-to-end and optimal ascent trajectory can be generated for the first stage of the vehicle.

A. Review of Endoatmospheric Algorithm

The relaxation approach used to numerically obtain the optimal endoatmospheric ascent trajectory is briefly reviewed here for the benefit of the reader (for more details, see [9]).

Denote $\boldsymbol{x} = (\,\boldsymbol{r}^T \quad \boldsymbol{V}^T\,)^T \in R^n$, $\boldsymbol{p} = (\,\boldsymbol{p}_r^T \quad \boldsymbol{p}_V^T\,)^T \in R^n$, and the augmented state vector of the optimal control problem $\boldsymbol{y} = (\,\boldsymbol{x}^T \quad \boldsymbol{p}^T\,)^T \in R^{2n}$ with $n = 6$. After replacing the control $\mathbf{1}_b$ using Eq. (21) or Eq. (26) and the corresponding $\mathbf{1}_N$ in the equations of motion (4) and (5) and costate equations (14) and (15), the two-point boundary-value problem (TPBVP) is now

$$\boldsymbol{y}' = \boldsymbol{f}(t, \boldsymbol{y}) \tag{40}$$

$$\boldsymbol{B}_0(\boldsymbol{y}_0) = 0 \tag{41}$$

$$\boldsymbol{B}_{cf}(\boldsymbol{y}_{cf}) = 0 \tag{42}$$

where $\boldsymbol{B}_0 = \boldsymbol{x}(t_0) - \boldsymbol{x}_0$ in our problem represents the given initial condition, and $\boldsymbol{B}_{cf}(\boldsymbol{y}_{cf}) = 0$ are the six conditions at the engine cutoff time t_{cf} of the first stage. These conditions will be further elaborated in Sec. V.C. The TPBVP is to find a solution $\boldsymbol{y}(t)$ that satisfies the differential equations (40) and boundary conditions (41) and (42). To find the solution, divide the time interval $t_{cf} - t_0$ into M subintervals of the same length $h = (t_{cf} - t_0)/M$. Let $\boldsymbol{y}_k = \boldsymbol{y}(t_0 + kh)$ be the value of the solution at the node $t_k = t_0 + kh$ $(k = 0, \ldots, M)$. At the middle point between t_{k-1} and t_k, denoted by $t_{k-1/2} = t_k - h/2$, the differential equations (40) are approximated by central finite difference:

$$\frac{1}{h}(\boldsymbol{y}_k - \boldsymbol{y}_{k-1}) = \boldsymbol{f}\left(t_{k-1/2}, \frac{\boldsymbol{y}_k + \boldsymbol{y}_{k-1}}{2}\right) \tag{43}$$

Or equivalently, $\boldsymbol{y}_k$ and $\boldsymbol{y}_{k-1}$ are constrained by the equation

$$\begin{gathered}\boldsymbol{E}_k(\boldsymbol{y}_k, \boldsymbol{y}_{k-1}) := \boldsymbol{y}_k - \boldsymbol{y}_{k-1} - h\boldsymbol{f}\left(t_{k-1/2}, \frac{\boldsymbol{y}_k + \boldsymbol{y}_{k-1}}{2}\right) = 0 \\ k = 1, \ldots, M-1\end{gathered} \tag{44}$$

In addition, the boundary conditions are denoted by

$$\boldsymbol{E}_0(\boldsymbol{y}_0) = \boldsymbol{B}_0(\boldsymbol{y}_0) = 0 \tag{45}$$

$$\boldsymbol{E}_M(\boldsymbol{y}_M) = \boldsymbol{B}_{cf}(\boldsymbol{y}_{cf}) = 0 \tag{46}$$

Treat $\boldsymbol{Y} = (\boldsymbol{y}_0^T \; \boldsymbol{y}_1^T \cdots \boldsymbol{y}_M^T)^T \in R^{2n(M+1)}$ as the unknowns. The same number of equations are

$$\boldsymbol{E}(\boldsymbol{Y}) = 0 \tag{47}$$

where $\boldsymbol{E} = (\boldsymbol{E}_0^T \; \boldsymbol{E}_1^T \cdots \boldsymbol{E}_M^T)^T$. Now the problem becomes a root-finding problem for a system of $2n(M+1)$ nonlinear algebraic equations (47). It turns out that the Jacobian of this system has a unique band structure that enables effective and efficient solution to the problem by a modified Newton–Raphson method that requires no computationally intensive inversion of the large Jacobian matrix [9].

B. Outline of Exoatmospheric Algorithm

Outside the dense atmosphere in which the aerodynamic forces can be safely ignored in the guidance solution, an analytical approach will be used to obtain the optimal exoatmospheric ascent trajectory for the upper stage(s) of the vehicle. The process is briefly outlined here, for completeness. For much more technical details, the reader is referred to [16].

Let us limit our discussion here to a two-stage vehicle, for clarity. The boundary conditions for the upper stage are the initial state condition $\boldsymbol{x}(t_{cf})$ (where, again, t_{cf} is the engine cutoff time of the first stage) and the orbital insertion condition and transversality conditions (from the optimal control theory) at the free final time t_f. The unknowns for the optimal ascent problem of the second stage are the initial costate $(\,\boldsymbol{p}_r(t_{cf}) \quad \boldsymbol{p}_V(t_{cf})\,)$ and the burn time $t_f - t_{cf}$. The problem is solved by a robust trust-region method as a root-finding problem [16]. The key points to be made here are that for a given initial condition $\boldsymbol{x}(t_{cf})$, the algorithm will very reliably find the optimal trajectory satisfying all the boundary conditions for the second stage, and the solution process will return the corresponding costate $(\,\boldsymbol{p}_r(t_{cf}) \quad \boldsymbol{p}_V(t_{cf})\,)$.

C. Algorithm Integration

The two algorithms reviewed in the last two sections need to work together to produce a complete optimal trajectory. In [11] a fixed-point iteration scheme is developed to iterate on the state at the burnout time t_{cf} of the first stage. The two algorithms are linked together to yield a continuous optimal trajectory when the fixed-point iteration converges. Although this approach is simple to implement and seems to work reasonably well, some additional initial guesses for the optimal condition at t_{cf} will be required as a part of the guidance I-loads. The convergence assurance of the fixed-point iteration process in all applications remains a persisting question, as it is well known that a contraction condition is needed for a fixed-point iteration to converge. Such a condition would be rather difficult, if not impossible, to come by because of the nature of the current problem. Hence, doubts may linger as to whether the approach will work the next time for a different vehicle or different mission profile. In the following, we provide a considerably improved integration scheme that links the two algorithms in a seamless fashion.

For any specified state $\boldsymbol{x}(t_{cf})$ at t_{cf}, the exoatmospheric algorithm will meet all the terminal constraints and return the corresponding costate $\boldsymbol{p}(t_{cf}) = (\boldsymbol{p}_r^T(t_{cf})\ \boldsymbol{p}_V^T(t_{cf}))^T$. Since $\boldsymbol{p}(t_{cf})$ is completely determined by $\boldsymbol{x}(t_{cf})$, no matter how many upper stages the vehicle has or whether coast arcs exist between two upper stages, $\boldsymbol{p}(t_{cf})$ may be viewed as a function of $\boldsymbol{x}(t_{cf})$, albeit numerical in nature. Denote this functional relationship by

$$\boldsymbol{p}_{cf}(\boldsymbol{x}(t_{cf})) = \boldsymbol{p}(t_{cf}) \tag{48}$$

In the finite difference (FD) solution process reviewed in Sec. V.A, $\boldsymbol{y}_M = \boldsymbol{y}_{cf} = (\boldsymbol{x}_M^T\ \boldsymbol{p}_M^T)^T$, where $\boldsymbol{x}_M$ is the state at t_{cf} and $\boldsymbol{p}_M$ is the costate at t_{cf}. For a specified $\boldsymbol{x}_M$, the exoatmospheric algorithm will produce the corresponding value of $\boldsymbol{p}_{cf}$. The continuity of the costate at t_{cf} requires that

$$\boldsymbol{p}_M - \boldsymbol{p}_{cf} = 0 \tag{49}$$

As discussed above, this $\boldsymbol{p}_{cf}$ is a function of $\boldsymbol{x}_M$, or $\boldsymbol{p}_{cf}(\boldsymbol{x}_M)$. Hence, the boundary condition in Eqs. (42) and (46) for the FD problem may be written in the explicit form of

$$\boldsymbol{E}_M(\boldsymbol{y}_M) = \boldsymbol{B}_{cf}(\boldsymbol{y}_{cf}) = \boldsymbol{p}_M - \boldsymbol{p}_{cf}(\boldsymbol{x}_M) = 0 \tag{50}$$

The evaluation of the gradients of $\boldsymbol{p}_{cf}(\boldsymbol{x}_M)$ with respect to the components of $\boldsymbol{x}_M$ will be needed in the numerical solution process, and it can be conveniently done numerically, as the exoatmospheric algorithm converges very rapidly and reliably. The functional dependence of Eq. (50) will not disrupt the band structure of the Jacobian of the algebraic system in Eq. (47). Thus, the same efficient algorithm can still be used to solve the FD problem.

In summary, in the current approach, the exoatmospheric ascent algorithm is embedded in the FD algorithm for endoatmospheric ascent through the equality condition in Eq. (50). There is no longer a need for additional I-loads for guessed conditions at t_{cf}. The convergence does not rely on convergence of a fixed-point iteration that is not verifiable a priori. This integration approach applies, regardless of whether there is just one upper stage or multiple upper stages or whether there is a coast arc in the flight of upper stage(s). After the separation of the first stage, the guidance of the upper stage(s) is performed by the exoatmospheric algorithm outlined in Sec. V.B.

VI. Application to Ares I Launch Vehicle

A. Vehicle Mission and Ascent Guidance

The Ares I crew launch vehicle is a two-stage vehicle currently under development by NASA that will carry the Orion Crew Exploration Vehicle (CEV) to the International Space Station (ISS). The first stage of the Ares I vehicle is a five-segment solid rocket booster (SRB) derived from the shuttle SRB. The vacuum thrust trace and mass flow rate of the SRB have quite strong dependence on time and cannot be approximated by constants. The separation of the SRB occurs when the thrust acceleration drops below 0.062 g (2.0 ft/s^2). The second-stage engine is a Saturn J-2-derived liquid engine, dubbed J2-X. Its thrust and mass flow rate are treated as constants in guidance [1]. A more detailed description of the modeling of the vehicle can be found in [18], and various data on the propulsion and aerodynamic models can be found in the simulation software SAVANT (which was implemented in [18]), of which early versions are publicly available.

In the simulations in this paper, 30 s after the ignition of the J2-X, the encapsulated service module panels and the launch abort system are jettisoned. The vehicle's gross liftoff weight is 918.6 t (about 2 million pounds) with a payload capacity of 25 t. The ISS mission target orbit for the Ares I is a -11×100 nm orbit (with an eccentricity of 0.0159) at the inclination of 51.6 deg. The insertion altitude into this orbit is specified at 70 nm. The CEV will use its own propulsion to reach the ISS orbit after separating from the Ares I. The orbital insertion conditions for the Ares I are summarized here:

$$\begin{aligned} r_f &= 6507.775\ \text{km}, \qquad & V_f &= 7797.6\ \text{m/s} \\ \gamma_f &= 0.8091\ \text{deg}, \qquad & i &= 51.6\ \text{deg} \end{aligned} \tag{51}$$

where γ_f is the inertial flight-path angle and V_f is the inertial velocity.

On the launch pad at the NASA Kennedy Space Center (KSC), the Ares I is positioned with the crew window facing due east. The launch will be heads-down for better crew visibility of the horizon. It will take about 6 s for the vehicle to vertically ascend to clear the tower. For the ensuing ascent guidance, both open-loop and closed-loop guidance will be performed in this section. The following describes the setting in each guidance mode used in the simulations in this paper:

1) With *open-loop guidance*, at $t_1 = 6$ s from liftoff, a complete optimized ascent trajectory with gravity turn is designed as described in Sec. IV.A, with $t_2 = 23.3$ s as the starting time of the gravity turn. The measured day-of-launch wind profile is included in the trajectory optimization (see the next section for more description on winds). The ascent-guidance commands for the first stage of the Ares I are extracted from this solution and then interpolated with respect to altitude in the simulation of the trajectory. Note that the ascent guidance for the second stage is still closed loop under the optimal exoatmospheric guidance algorithm in [16].

2) With *closed-loop guidance*, the endoatmospheric guidance algorithm with the implementation in Sec. IV.B for bending-moment constraint enforcement is called in each guidance cycle to compute the ascent-guidance commands for the first stage (and the

exoatmospheric guidance algorithm in [16] is also used for the second stage).

The day-of-launch wind profile is included in the process of each solution. The following constraint is imposed in the guidance solution until the cutoff of the SRB:

$$\alpha_t \bar{q} \leq n_{q_{\max}} \tag{52}$$

The value of $n_{q_{\max}}$ can be regarded as a guidance design parameter. The choice of its value obviously should be less than the actual limit of $\alpha_t \bar{q}$ imposed on the vehicle, but also dependent on the fidelity of the wind model used in the guidance solution. It can be tightened (reduced) if the actual peak $\alpha_t \bar{q}$ in the presence of winds and other dispersions is considered too high, or it may be relaxed for increased injected mass if the dispersed peak $\alpha_t \bar{q}$ is well below the limit. The value of $n_{q_{\max}} = 800$ psf-deg is used as the nominal in the simulations for the Ares I in this paper, unless otherwise stated. The rationale for this choice is that for the wind profiles used in this paper, this value suffices to allow the closed-loop guidance to meet the actual bending-moment constraint for the Ares I (see Secs. VI.B and VI.C for more information).

The closed-loop guidance is applied as soon as the Ares I clears the tower at $t_1 = 6$ s. There is no explicit requirement for flying a gravity-turn trajectory. The vehicle flies whatever constrained trajectory the optimal guidance decides.

In both closed-loop and open-loop guidance modes, the guidance update rate is 1 Hz, and the trajectory simulation is performed at 100 Hz. In all simulations, a pitch-angle rate limit of 2.5 deg/s is enforced on the guidance command sent to the 3-DOF simulation so that the performance is assessed on a more realistic basis.

B. Winds and Dispersions in Propulsion and Other Parameters

One of the important measures used to evaluate the performance of ascent guidance for the Ares I is wind-induced load. For testing purposes, 114 different wind profile pairs for the month of February are used, which are based on measurement data at KSC. These wind profiles are generated by the Natural Environments Branch at NASA Marshall Space Flight Center. Each profile provides altitude-dependent wind speed and direction. The first of each pair is a smoothed (filtered) profile of measured wind data [19]; the second is unfiltered and measured, on average, 2 h later. The smoothed profile in each pair is used in the guidance solution, and the unfiltered profile is used in simulation of the trajectory. In Monte Carlo simulations, the wind pair is randomly selected in uniform distribution for a trajectory to simulate the day-of-launch wind. In the flight, dispersed by winds and other uncertainty, it is required for the guidance to keep the actual $\alpha_t \bar{q}$ below the limit

$$\alpha_t \bar{q} \leq 3000 \text{ (psf-deg)} \tag{53}$$

Since the true α_t depends on the actual wind, which will not be identical to the filtered wind used in guidance, the closed-loop guidance will still use the target value 800 psf-deg, as given in Eq. (52), instead of 3000 psf-deg. In so doing, the guidance leaves adequate margin to accommodate the difference between the actual wind and the model of the wind (filtered wind).

Another source of significant dispersions is on the thrust and mass flow rate characteristics of the SRB. For a specified day and month of launch from the KSC, the nominal time-dependent thrust trace and mass rate of the SRB are scaled by factors dependent on the dispersions of propellant mean bulk temperature (PMBT), propellant burn rate, and propellant loading to simulate the actual SRB thrust trace and mass rate. The dispersions in PMBT and propellant burn rate are modeled by Gaussian distributions. In the time-dependent scaling, while the percentages of the thrust and mass rate dispersions can be appreciable (so the burn time of the SRB will be different as a consequence), the specific impulse of the SRB is kept within 1% of its nominal value (hence, the total impulse imparted by the SRB remains nearly constant, even though the thrust magnitude at any given time and burn time may be different: this is a property that should be kept in mind when viewing the results of dispersion simulations in subsequent sections). The ratio of the actual propellant loading of the SRB to its nominal value is also dispersed with a Gaussian distribution of unity-mean and 3-sigma of 0.0025 (±0.25%). The thrust of the J2-X engine of the second stage is dispersed in zero-mean Gaussian distribution with a 3-sigma value of 0.8% of its nominal thrust. In addition, the I_{sp} of the J2-X engine is dispersed by a zero-mean Gaussian distribution of 3-sigma value of 2.2 s.

The nominal aerodynamic coefficients of the vehicle (which are functions of Mach number and angle of attack) are used by the guidance, but dispersed values up to ±10% in uniform distributions are used in the simulations to simulate aerodynamic uncertainty. No navigation dispersions are considered in the simulations. Inclusion of navigation uncertainty would chiefly affect the orbital insertion precision, but not other concerns such as performance and aerodynamic load.

C. Performance of Closed-Loop Guidance

All the results presented from here on are from closed-loop 3-DOF simulations. First, the nominal ascent without winds and other dispersions added is examined. Two cases are compared. One is fully constrained, subject to Eq. (52) with $n_{q_{\max}} = 800$ and guided by closed-loop guidance starting at $t_1 = 6$ s. The other is freely optimized after the vertical ascent at $t_1 = 6$ s, without the $\alpha_t \bar{q}$ constraint in Eq. (52). Figure 2 shows the angle-of-attack profiles for the two trajectories. The solid line is for the constrained trajectory. It can seen that the constrained α profile is qualitatively similar to that of the α in [1], which is from a gravity-turn trajectory optimized offline and essentially the same as the result obtained from POST

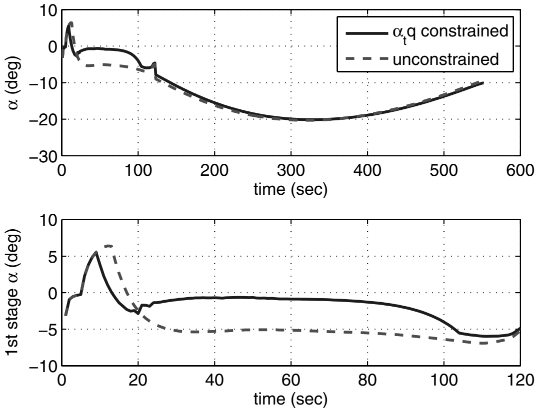

Fig. 2 Angle of attack along nominal optimal ascent trajectories; α along the complete trajectory (top) and α for the first stage (inside the atmosphere) (bottom).

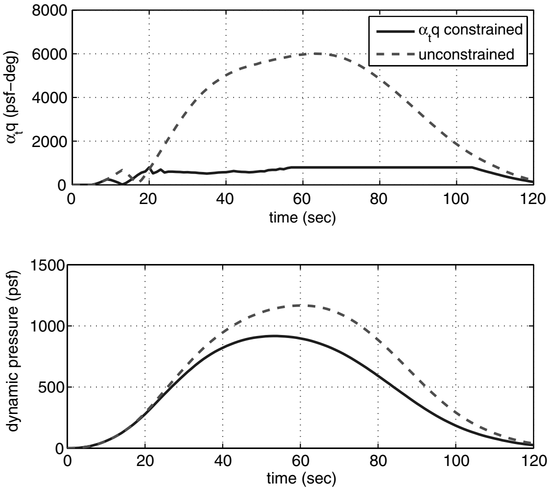

Fig. 3 $\alpha_t \bar{q}$ and dynamic pressure $\bar{q}$ along the nominal optimal ascent trajectories of the first stage.

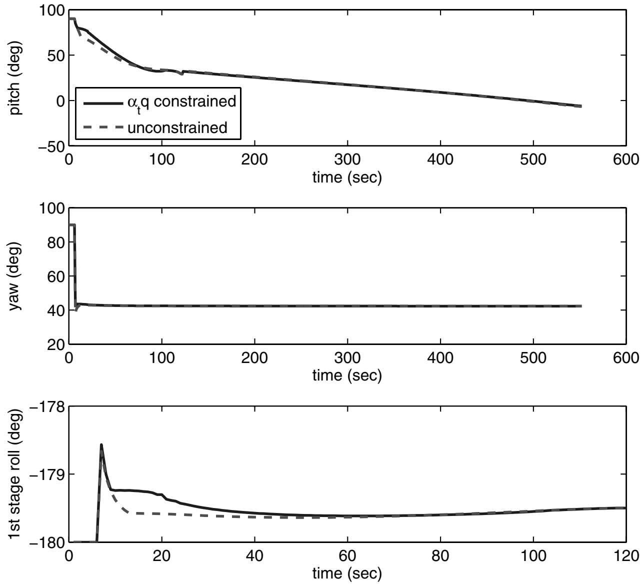

Fig. 4 Euler angles with respect to the launch NED frame along nominal optimal ascent trajectories.

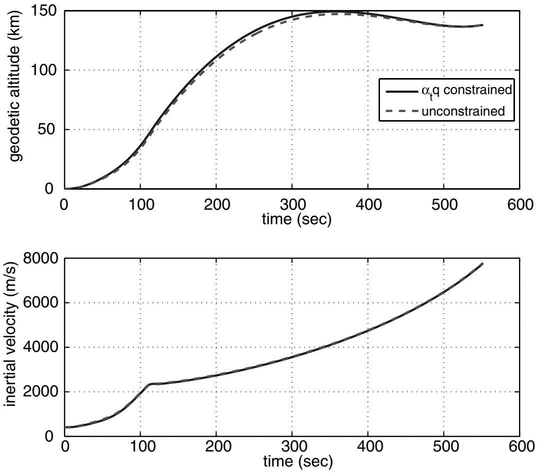

Fig. 5 Altitude and velocity along nominal optimal ascent trajectories.

[20]. The difference is that the constrained α profile in Fig. 2 is not exactly zero after 23.3 s, since the closed-loop guidance is not aimed at achieving a strict gravity turn. On the other hand, after the initial vertical ascent, the *unconstrained* optimal trajectory flies an α of approximately -5 deg (about seven times that of the constrained one) throughout the atmospheric ascent. Yet the second-stage α profiles of the two trajectories are very close to each other. The corresponding $\alpha_t\bar{q}$ and dynamic pressure $\bar{q}$ during the first stage are plotted in Fig. 3. It is seen that the unconstrained trajectory experiences a peak $\alpha_t\bar{q}$ of about 6000 psf-deg, more than seven times that along the constrained trajectory. However, the penalty for flying this highly constrained trajectory is an approximate 195 kg reduction in the injected mass, or a 0.44% reduction compared with the unconstrained one. This is quite remarkable, considering the severity of the constraint. This achievement demonstrates the effectiveness and importance of proper optimization of the constrained ascent guidance.

Figure 4 shows the comparison of the Euler angles of the vehicle's body axes during the nominal ascent. These angles are with respect to the north–east–down (NED) coordinate system at the launch site, in the standard yaw–pitch–roll rotation sequence. Again, the comparison is very close, except for some difference in the pitch angle during atmospheric portion of the trajectories that show that the unconstrained trajectory pitches over a little faster. Because the crew window faces downrange at launch, the equations for heads-down launch in Eqs. (25–27) are used in computing the optimal body axes. Not surprisingly, the optimal yaw angle found is practically constant and only about 2.5 deg different from the usual launch azimuth:

$$\psi_{az} = \sin^{-1}\left(\frac{\cos i}{\cos \phi_c}\right)$$

where i is the target orbit inclination, and ϕ_c the geocentric latitude of the launch site. The roll angle stays very close to 180 deg (for heads-down launch) throughout the entire ascent. Figure 5 illustrates the altitude and velocity profiles of the nominal ascent with and without the $\alpha_t\bar{q}$ constraint (52). The difference in velocity is indiscernible in the scale of the figure, and the largest altitude difference is about 4 km. This altitude difference counts for the fact the constrained trajectory has to fly higher at the same velocity in order to satisfy the constraint in Eq. (52).

The small differences observed in Figs. 2–5 between the constrained and unconstrained nominal trajectories serve as a reassuring indication that the highly constrained trajectory is indeed properly optimized.

Next, 1000 dispersed trajectories are simulated with the dispersions and winds described in Sec. VI.B. In each simulation, the guidance is given only the nominal models of the vehicle, propulsion systems, and atmosphere, plus the smoothed (and two-hour-earlier) profile of the randomly selected day-of-launch wind profile. No additional guidance I-loads are adjusted from one trajectory to another, and no prelaunch guidance computation or update is performed.

The statistics on some of the trajectory parameters and final (orbital insertion) conditions are listed in Table 1. Also included in Table 1 are the statistics of the peak values of $\alpha_t\bar{q}$ along all these trajectories. Instead of listing the maximum and minimum of each parameter, 99.73- and 0.27-percentile values are shown. This is done to reduce the effects of extreme outliers in the statistics.

Compared with the required values in Eq. (51), the data in Table 1 clearly demonstrate accurate orbital insertion conditions and quite consistent performance in terms of injected mass. The high accuracy of the orbital insertion conditions seen in the table suggests that if navigation errors are included, the orbital insertion errors will be on the same order as that of the navigation errors. This high accuracy should also be viewed in the context that no effects of the uncertainty

Table 1 Statistics of 1000 dispersed closed-loop optimally guided trajectories with $n_{q_{\max}} = 800$ psf-deg: final conditions and peak $\alpha_t\bar{q}$

	Mean	Std. deviation	99.73-percentile	0.27-percentile
Radius r_f, m	6,507,775.0	0.53	6,507,771.1	6,507,773.3
Inertial velocity V_f, m/s	7,797.78	0.10	7,798.00	7,797.31
Inertial flight-path angle γ_f, deg	0.8091	0.0054	0.8261	0.7857
Inclination i, deg	51.6000	0.00001	51.6001	51.5999
Semimajor axis a, m	6,460,814.1	170.9	6,462,121.4	6,460,111.5
Eccentricity e	0.01589	0.00008	0.01609	0.01564
SRB burn time, s	122.97	1.23	126.00	119.20
Flight time, s	552.32	0.93	554.85	549.35
Injected mass m_f, kg	44,326.7	147.3	44,709.6	43,974.9
Peak $\alpha_t\bar{q}$, psf-deg	1,534.3	383.3	2,901.6	867.6

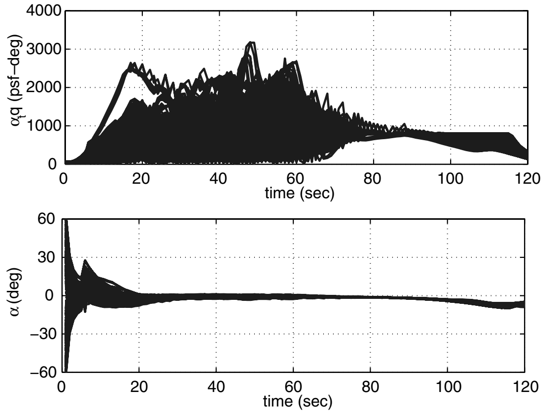

Fig. 6 **Variations of first-stage $\alpha_t\bar{q}$ and α along 1000 dispersed closed-loop optimally guided ascent trajectories.**

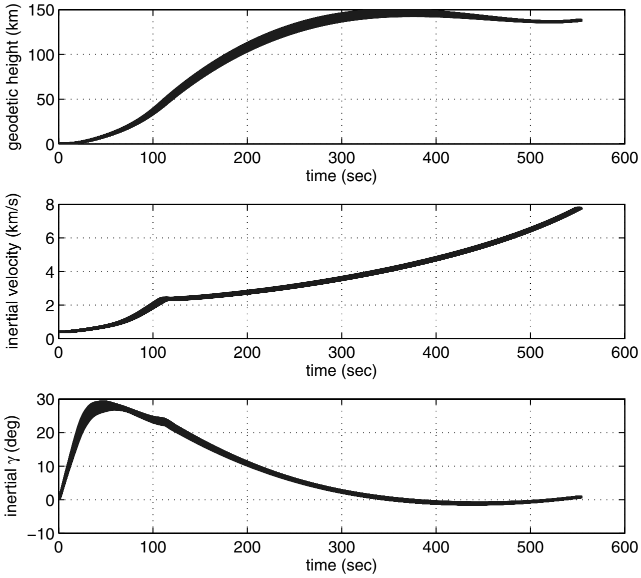

Fig. 7 **Geodetic altitude, inertial velocity and inertial flight-path angle along 1000 dispersed closed-loop optimally guided ascent trajectories.**

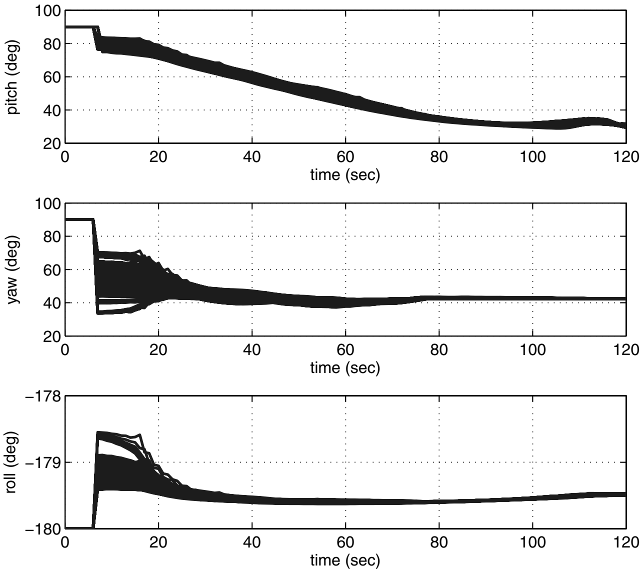

Fig. 8 **Variations of first-stage Euler angles with respect the launch NED frame along 1000 dispersed closed-loop optimally guided ascent trajectories.**

Table 2 **Statistics of 1000 dispersed closed-loop optimally guided trajectories with reduced $n_{q_{\max}} = 500$ psf-deg: final mass and peak $\alpha_t\bar{q}$**

	Mean	Std. deviation	99.73-percentile	0.27-percentile
Injected mass m_f, kg	44,247.4	198.1	44,634.5	42,898.6
Peak $\alpha_t\bar{q}$, psf-deg	1,279.7	371.1	2,488.9	598.9

caused by tail-off thrust of the J2-X engine are included when it is commanded to shut off. Such an uncertainty can cause, for instance, the error of a few nautical miles in semimajor axis of the final orbit. Again, one of the most critical concerns during atmospheric ascent is the bending moment in the presence of the winds. The statistics on peak $\alpha_t\bar{q}$ shows that the 99.73-percentile value of 2900 psf-deg is within the required limit of 3000 psf-deg. There are two cases in which the maximum peak $\alpha_t\bar{q}$ reaches about 3180 psf-deg (not shown in the table, because they fall outside 99.73-percentile). The first subplot in Fig. 6 clearly shows the same conclusion. The second subplot of Fig. 6 shows that the optimal closed-loop guidance automatically keeps the angle of attack small whenever necessary during the flight of the first stage. Under the closed-loop guidance, the accuracy of enforcing the $\alpha_t\bar{q}$ constraint is almost entirely dependent on how well the measured wind profiles used in the guidance solutions match the winds encountered in the actual flight (in the simulations, this means the difference between the filtered wind profile and nonfiltered profile).

The geodetic altitude, inertial velocity, and inertial flight-path-angle variations along the 1000 trajectories are plotted in Fig. 7. The Euler angles of the vehicle body axes with respect to the launch NED frame during the first-stage ascent are depicted in Fig. 8.

If additional margins in enforcing the bending-moment constraint in Eq. (53) are desired, the parameter $n_{q_{\max}}$ in Eq. (52) can be further reduced. To demonstrate its effects, $n_{q_{\max}} = 500$ psf-deg is used in the guidance solution for the same 1000 dispersed trajectories. The statistics for the final orbital insertion conditions are essentially the same as in Table 1, but different for the final injected mass and peak $\alpha_t\bar{q}$ value, which are listed in Table 2. In comparison with the cases with $n_{q_{\max}} = 800$ psf-deg in Table 1, the peak $\alpha_t\bar{q}$ is now noticeably lowered. In fact, the highest peak $\alpha_t\bar{q}$ is just 2870 psf-deg (outside 99.73-percentile and not shown in Table 2), and the 99.73-percentile value is well below the 3000 psf-deg limit. On the other hand, the penalty for flying a more stringently constrained trajectory is reduced injected mass, with an average reduction of 79 kg. But more pronounced is the 1000 kg reduction in the 0.27-percentile injected mass. These differences simply reflect the classical tradeoff between performance and constraints.

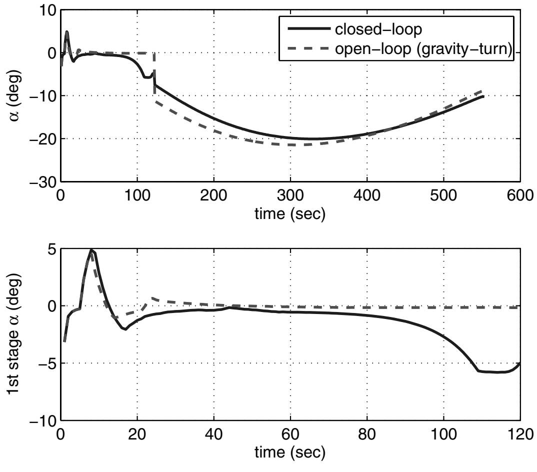

Fig. 9 **Comparison of α along nominal optimal (non-gravity-turn) ascent trajectories; α along the complete trajectories (top) and α for the first stage (inside the atmosphere) (bottom).**

Table 3 Statistics of 1000 dispersed trajectories under open-loop guidance for the first stage: final mass and peak $\alpha_t\bar{q}$

	mean	std. deviation	99.73-percentile	0.27-percentile
Injected mass m_f, kg	44,141.7	128.2	44,464.9	43,834.5
Peak $\alpha_t\bar{q}$, psf-deg	1,392.0	388.4	2,868.2	647.8

D. Comparison with Open-Loop Guidance

Recall from the description of the open-loop guidance mode in Sec. VI.A that the only difference between the open-loop-guided and closed-loop-guided trajectories lies in the endoatmospheric ascent guidance. Figure 9 shows the α profiles along the nominal open-loop- and closed-loop-guided trajectories. The gravity turn after 23.3 s is signified by the zero α along the open-loop-guided trajectory. Still, for the most part, the two α profiles for the first stage are quite similar, despite the fact that the closed-loop guidance is not explicitly required to do a gravity turn. The open-loop-guided α profile is very similar to that in Fig. 1 of [1].

To see how conventional open-loop endoatmospheric ascent guidance compares with closed-loop guidance, the same 1000 dispersed trajectories are resimulated. Everything is the same in trajectory simulations, from the dispersions and winds to separation events. But the guidance for the first stage is now *open-loop*. Thus, the differences between these open-loop-guided and previous closed-loop-guided trajectories are completely the results of the difference in endoatmospheric guidance.

The statistics on injected mass and peak $\alpha_t\bar{q}$ along the 1000 dispersed trajectories are summarized in Table 3 (the orbital insertion statistics are very similar to those in Table 1, because the second-stage guidance is still closed-loop). Compared with closed-loop guidance, the statistics on peak $\alpha_t\bar{q}$ are about the same: in particular, the 99.73-percentile value. Figure 10 shows the variations of $\alpha_t\bar{q}$ and α along these 1000 trajectories. Similar to Fig. 6, it can be seen that two of the 1000 trajectories exceed the 3000 psf-deg limit in $\alpha_t\bar{q}$ (with the maximum over 3300 psf-deg). The mean injected mass under open-loop guidance is 185 kg lower than under closed-loop guidance. The reduction of average injected mass under open-loop guidance is partially attributable to the gravity-turn trajectory, which is highly restrictive (but it is necessary for open-loop guidance; otherwise, the $\alpha_t\bar{q}$ constraint would be grossly violated in the presence of winds). Although 185 kg do not seem to be a substantial amount in absolute terms, recall from Sec. VI.C that the difference in injected mass between the constrained and unconstrained optimal trajectories is 195 kg. To put this in another perspective, the performance gained by optimal closed-loop guidance is about the same as the performance gained by completely removing the bending-moment constraint. This perspective carries an implication on performance advantage that will be more striking in terms of kilograms for vehicles with higher lift-to-drag ratios (such as reusable launch vehicles).

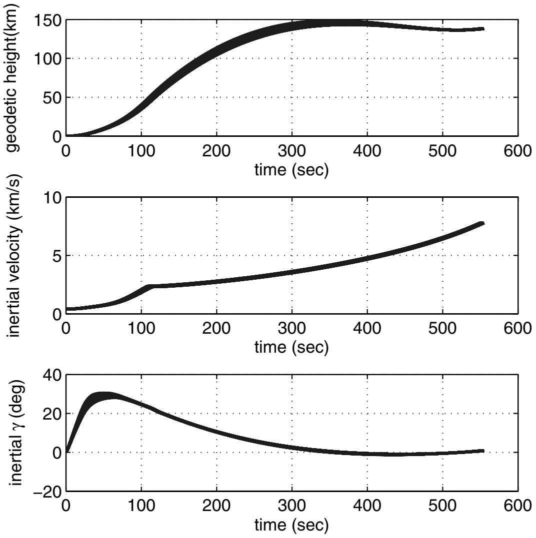

Fig. 11 Geodetic altitude, inertial velocity, and inertial flight-path angle along 1000 dispersed open-loop-guided ascent trajectories.

The geodetic altitude, inertial velocity, and inertial flight-path-angle histories of the 1000 trajectories are plotted in Fig. 11. The pitch, yaw, and roll angle variations of the vehicle during the first stage with respect to the NED frame are illustrated in Fig. 12. Comparison of these profiles with those under closed-loop guidance in Figs. 7 and 8 shows strong similarities.

We also experimented with doubling the SRB dispersions while keeping winds and other dispersions the same. Both closed-loop and open-loop endoatmospheric ascent guidance are tested again. Table 4 summarizes the statistics on the injected mass and peak $\alpha_t\bar{q}$ along the 1000 dispersed trajectories. Although the average injected mass under both guidance approaches remains about the same as before, the spread of the injected masses is considerably larger, signified by the nearly tripled standard deviations. This outcome is no surprise, as larger dispersions in SRB directly contribute to larger injected mass variations. The real differentiating factor is on the peak $\alpha_t\bar{q}$. The closed-loop guidance essentially achieves the same statistics on peak $\alpha_t\bar{q}$ as in Table 1; even the two outliers of the highest values of peak $\alpha_t\bar{q}$ remain about the same (at 3200 psf-deg; not shown in the table). Under open-loop guidance, however, the 99.73-percentile peak $\alpha_t\bar{q}$ is about 400 psf-deg higher than that in Table 3: over 10% above the required limit. In fact, the highest peak $\alpha_t\bar{q}$ (not shown in the table) is as high as 4044 psf-deg. The evidence suggests that closed-loop guidance is able to provide much more consistent bending-moment constraint enforcement in the presence of large SRB dispersions.

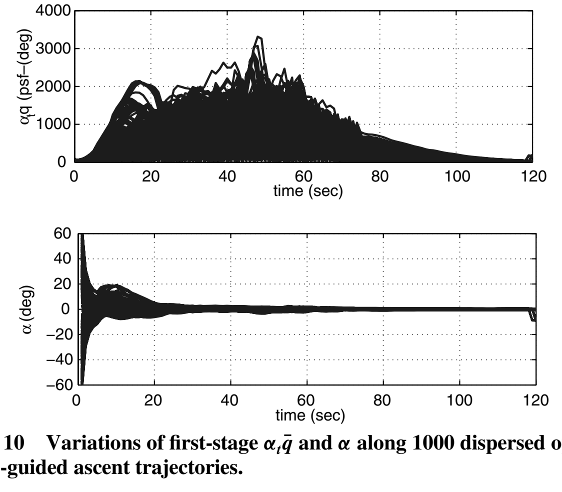

Fig. 10 Variations of first-stage $\alpha_t\bar{q}$ and α along 1000 dispersed open-loop-guided ascent trajectories.

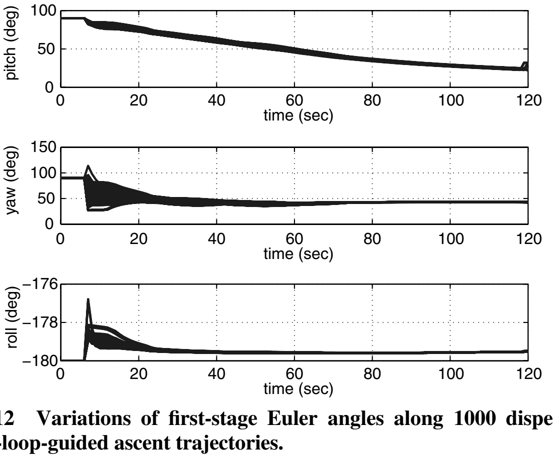

Fig. 12 Variations of first-stage Euler angles along 1000 dispersed open-loop-guided ascent trajectories.

Table 4 Statistics of 1000 dispersed trajectories under different first-stage guidance approaches with doubled SRB dispersions

First-stage guidance	Parameter	Mean	Std. deviation	99.73-percentile	0.27-percentile
Closed-loop guidance	m_f, kg	44,301.8	427.1	45,308.0	42,931.6
Closed-loop guidance	Peak $\alpha_t\bar{q}$, psf-deg	1,529.3	387.1	2,977.1	846.9
Open-loop guidance	m_f, kg	44,130.7	362.8	45,053.5	43,176.4
Open-loop guidance	Peak $\alpha_t\bar{q}$, psf-deg	1,549.2	471.2	3,311.6	684.2

VII. Conclusions

This paper represents the latest effort on optimal ascent guidance for multiple-stage launch vehicles tightly constrained by an aerodynamic bending-moment limit. Although traditional first-stage ascent guidance for such cases relies on gravity turn under open-loop guidance, it is always an open question as to what, if any, potential advantages can be gained by employing closed-loop endoatmospheric ascent guidance. But there is a scarcity of literature in this regard, probably due in large part to the lack of a reliable and fast algorithm to solve the constrained optimal endoatmospheric ascent problem. The new developments in this paper afford just such a capability and enable us to conduct an extensive comparative study of optimal closed-loop and traditional open-loop ascent guidance using the vehicle and mission data of the Ares I launch vehicle. The evidence from this study clearly demonstrates that optimal closed-loop guidance indeed outperforms optimized gravity-turn ascent under open-loop guidance in terms of injected mass. The key for achieving this advantage, however, lies in correctly enforcing the aerodynamic bending constraint as *an integral part* of the optimal guidance solution, rather than handling it in a load-relief measure outside the optimization process. In the presence of larger dispersions affecting endoatmospheric ascent, closed-loop ascent guidance is also superior to open-loop guidance in maintaining a consistent performance in satisfying the bending-moment constraint.

It should be noted that the specifics of advantages of closed-loop ascent guidance over open-loop ascent guidance reported this paper are intimately tied to the Ares I vehicle. The Ares I is an axisymmetric vehicle flying at a very small angle attack for most of the atmospheric ascent. As such, the aerodynamic force is mainly in the form of drag (or axial force). For other types of launch vehicles with more significant aerodynamic lift (or normal force) and allowed to fly higher angles of attack, it is very reasonable to expect that closed-loop guidance will enjoy even better performance in injected mass under the same conditions. When onboard wind-speed measurements become available, closed-loop guidance will be in the best position to use real-time wind data in the guidance solution, potentially dramatically enhancing the safety of the launch vehicle on aerodynamic-load-related concerns.

Acknowledgment

The author at Iowa State University thanks Gregory Dukeman of NASA Marshall Space Flight Center for stimulating discussions and exchanges related to the subject matters in this paper.

References

[1] Dukeman, G. A., and Hill, A., "Rapid Trajectory Optimization for the Ares I Launch Vehicle," AIAA Paper 2008-6288, Aug. 2008.

[2] Brown, K. R., Harrold, E. F., and Johnson, G. W., "Some New Results on Space Shuttle Atmospheric Ascent Optimization," AIAA Paper 70-978, 1970.

[3] Vinh, N. X., "General Theory of Optimal Trajectory for Rocket Flight in a Resisting Medium," *Journal of Optimization Theory and Applications*, Vol. 11, No. 2, 1973, pp. 189–202. doi:10.1007/BF00935883

[4] Corvin, M. A., "Ascent Guidance for a Winged Boost Vehicle," NASA CR-172083, Aug. 1988.

[5] Leung, M. S. K., and Calise, A. J., "Hybrid Approach to Near-Optimal Launch Vehicle Guidance," *Journal of Guidance, Control, and Dynamics*, Vol. 17, No. 5, 1994, pp. 881–888. doi:10.2514/3.21285

[6] Calise, A. J., Melamed, N., and Lee, S., "Design and Evaluation of a Three-Dimensional Optimal Ascent Guidance Algorithm," *Journal of Guidance, Control, and Dynamics*, Vol. 21, No. 6, 1998, pp. 867–875. doi:10.2514/2.4350

[7] Gath, P. F., and Calise, A. J., "Optimization of Launch Vehicle Ascent Trajectories with Path Constraints and Coast Arcs," *Journal of Guidance, Control, and Dynamics*, Vol. 24, No. 2, 2001, pp. 296–304. doi:10.2514/2.4712

[8] Dukeman, G. A., "Atmospheric Ascent Guidance for Rocket-Powered Launch Vehicles," AIAA Paper 2002-4559, Aug. 2002.

[9] Lu, P., Sun, H., and Tsai, B., "Closed-Loop Endo-Atmospheric Ascent Guidance," *Journal of Guidance, Control, and Dynamics*, Vol. 26, No. 2, 2003, pp. 283–294. doi:10.2514/2.5045

[10] Dukeman, G. A., and Calise, A. J., "Enhancements to an Atmospheric Ascent Guidance Algorithm," AIAA Paper 2003-5638, Aug. 2003.

[11] Lu, P., Zhang, L., and Sun, H., "Ascent Guidance for Responsive Launch: A Fixed-Point Approach," AIAA Paper 2005-6453, Aug. 2005.

[12] Dukeman, G. A., "Closed-Loop Nominal and Abort Atmospheric Ascent Guidance for Rocket-Powered Launch Vehicles," Ph.D. Dissertation, Georgia Inst. of Technology, Atlanta, May 2005.

[13] Johnson, E. N., Calise, A. J., Curry, M. D., Mease, K. D., and Corban, J. E., "Adaptive Guidance and Control for Autonomous Hypersonic Vehicles," *Journal of Guidance, Control, and Dynamics*, Vol. 29, No. 3, 2006, pp. 725–737. doi:10.2514/1.14767

[14] Hanson, J. M., Shrader, M. W., and Cruzen, C. A., "Ascent Guidance Comparisons," *Journal of the Astronautical Sciences*, Vol. 43, No. 3, 1995, pp. 307–326.

[15] Lawden, D. F., *Optimal Trajectories for Space Navigation*, Butterworth, London, 1963, pp. 54–68.

[16] Lu, P., Griffin, B., Dukeman, G., and Chavez, F., "Rapid Optimal Multiburn Ascent Planning and Guidance," *Journal of Guidance, Control, and Dynamics*, Vol. 31, No. 6, 2008, pp. 1656–1664. doi:10.2514/1.36084

[17] Pontryagin, L. S., Boltyanskii,V. G., Gramkreledze, Q. V., and Mishchenko, E. F., *The Mathematical Theory of Optimal Processes*, Intersciences, New York, 1962, pp. 20–21, 311–316.

[18] Betts, K. M., Rutherford, R. C., McDuffie, J., Johnson, M. D., Jackson, M., and Hall, C., "Time Domain Simulation of the NASA Crew Launch Vehicle," AIAA Paper 2007-6621, Aug. 2007.

[19] Graham, R. J., "Determination and Analysis of Numerical Smoothing Weights," NASA TR R-179, 1963.

[20] Brauer, G., Cornick, D., Habeger, A., and Peterson, F., "Program to Optimize Simulated Trajectories (POST). Volume 3: Programmer's Manual," Martin Marietta Corp., Denver, CO, April 1975.